JGR Solid Earth

RESEARCH ARTICLE
10.1029/2020JB019964

Key Points:
- Bridgmanite may contain 50% trivalent cations through Fe^{3+}-Al^{3+} coupled substitution
- The bulk sound velocity of $(Mg_{0.5}Fe^{3+}_{0.5})(Al_{0.5}Si_{0.5})O_3$ bridgmanite is 7.7% lower than $MgSiO_3$
- Through Fe-Al cation exchange, Fe^{3+} in $(Mg_{0.5}Fe^{3+}_{0.5})(Al_{0.5}Si_{0.5})O_3$ bridgmanite undergoes gradual spin transition at lower mantle conditions

Supporting Information:
- Supporting Information S1

Correspondence to:
B. Chen and J. Li,
binchen@hawaii.edu;
jackieli@umich.edu

Citation:
Zhu, F., Liu, J., Lai, X., Xiao, Y., Prakapenka, V., & Bi, W., et al. (2020). Synthesis, elasticity, and spin state of an intermediate $MgSiO_3$-$FeAlO_3$ bridgmanite: Implications for iron in Earth's lower mantle. *Journal of Geophysical Research: Solid Earth*, *125*, e2020JB019964. https://doi.org/10.1029/2020JB019964

Received 10 APR 2020
Accepted 18 JUN 2020
Accepted article online 22 JUN 2020

Synthesis, Elasticity, and Spin State of an Intermediate $MgSiO_3$-$FeAlO_3$ Bridgmanite: Implications for Iron in Earth's Lower Mantle

Feng Zhu[1,2], Jiachao Liu[1,3], Xiaojing Lai[2,4], Yuming Xiao[5], Vitali Prakapenka[6], Wenli Bi[7,8,9], E. Ercan Alp[7], Przemyslaw Dera[2], Bin Chen[2], and Jie Li[1]

[1]Earth and Environmental Sciences, University of Michigan, Ann Arbor, MI, USA, [2]Hawai'i Institute of Geophysics and Planetology, University of Hawai'i at Mānoa, Honolulu, HI, USA, [3]Earth and Environmental Sciences, Michigan State University, East Lansing, MI, USA, [4]Gemmological Institute, China University of Geosciences, Wuhan, China, [5]HPCAT, Advanced Photon Source, Argonne National Laboratory, Argonne, IL, USA, [6]Center for Advanced Radiation Sources, University of Chicago, Argonne, IL, USA, [7]Advanced Photon Source, Argonne National Laboratory, Argonne, IL, USA, [8]Department of Geology, University of Illinois at Urbana-Champaign, Urbana, IL, USA, [9]Department of Physics, University of Alabama at Birmingham, Birmingham, AL, USA

Abstract Fe-Al-bearing bridgmanite may be the dominant host for ferric iron in Earth's lower mantle. Here we report the synthesis of $(Mg_{0.5}Fe^{3+}_{0.5})(Al_{0.5}Si_{0.5})O_3$ bridgmanite (FA50) with the highest Fe^{3+}-Al^{3+} coupled substitution known to date. X-ray diffraction measurements showed that at ambient conditions, the FA50 adopted the $LiNbO_3$ structure. Upon compression at room temperature to 18 GPa, it transformed back into the bridgmanite structure, which remained stable up to 102 GPa and 2,600 K. Fitting Birch-Murnaghan equation of state of FA50 bridgmanite yields $V_0 = 172.1(4)$ Å^3, $K_0 = 229(4)$ GPa with $K_0' = 4$(fixed). The calculated bulk sound velocity of the FA50 bridgmanite is ~7.7% lower than $MgSiO_3$ bridgmanite, mainly because the presence of ferric iron increases the unit-cell mass by 15.5%. This difference likely represents the upper limit of sound velocity anomaly introduced by Fe^{3+}-Al^{3+} substitution. X-ray emission and synchrotron Mössbauer spectroscopy measurements showed that after laser annealing, ~6% of Fe^{3+} cations exchanged with Al^{3+} and underwent the high- to low-spin transition at 59 GPa. The low-spin proportion of Fe^{3+} increased gradually with pressure and reached 17–31% at 80 GPa. Since the cation exchange and spin transition in this Fe^{3+}-Al^{3+}-enriched bridgmanite do not cause resolvable unit-cell volume reduction, and the increase of low-spin Fe^{3+} fraction with pressure occurs gradually, the spin transition would not produce a distinct seismic signature in the lower mantle. However, it may influence iron partitioning and isotopic fractionation, thus introducing chemical heterogeneity in the lower mantle.

Plain Language Summary Fe-Al-bearing bridgmanite may be the dominant mineral in the lower mantle, which occupies more than half of Earth's volume. A subject of much debate is whether spin transition of Fe in bridgmanite produces an observable influence on the physics and chemistry of the lower mantle. In this study, we synthesized a new $(Mg_{0.5}Fe^{3+}_{0.5})(Al_{0.5}Si_{0.5})O_3$ bridgmanite with the highest Fe^{3+}-Al^{3+} coupled substitution known to date. We studied its structure, elasticity, and spin state by multiple experimental and theoretical methods. The high Fe content allowed us to better resolve a pressure-induced spin transition of Fe^{3+} caused by Fe-Al cation exchange at high temperature. Our results suggest that the spin transition is enabled by cation exchange but has a minor effect on the seismic velocity, although it may introduce chemical heterogeneity in the lower mantle. Our study helps resolve existing discrepancies on the nature of spin transition of Fe-Al bridgmanite and its influence on the physics and chemistry of the lower mantle.

1. Introduction

Bridgmanite is the dominant phase in the Earth's lower mantle (Tschauner et al., 2014). It has an ABX_3-type perovskite structure, consisting of eight corner-sharing BX_6 octahedra with a larger A cation caged in the center AX_{8-12} pseudo-dodecahedral site. The main composition of bridgmanite is $MgSiO_3$, but it can also accommodate a considerable amount of Fe^{2+} in its A site and coupled Fe^{3+} and Al^{3+} in its A and B sites

for charge balance (Andrault et al., 2001; Boffa Ballaran et al., 2012; Glazyrin et al., 2014; Nishio-Hamane et al., 2005, 2008). Therefore, its actual chemical composition in the Earth's lower mantle can vary within the formula (Mg, Fe^{2+}, Fe^{3+}, Al)(Si, Al, Fe^{3+})O_3 depending on different bulk composition, pressure (P), temperature (T), and oxygen fugacity (f_{O2}). Frost et al. (2004) showed that Fe^{2+} in bridgmanite underwent a self-disproportionation at lower mantle P–T conditions, elevating the concentration of Fe^{3+} in bridgmanite. Since most peridotitic and basaltic sources have a higher than unity Al/Fe ratio (Mohn & Trønnes, 2016), and Fe^{3+}-Al^{3+} coupled substitution is the favored mechanism to incorporate trivalent cations into bridgmanite (Andrault et al., 2001; Mohn & Trønnes, 2016; Nishio-Hamane et al., 2005), the Fe-Al bridgmanite can be a dominant phase to host Fe and Al in the lower mantle (Wang et al., 2015).

As the only major element with variable valence and potential magnetic transition in bridgmanite, iron plays a key role on its elastic and electrical properties. It may also influence element partitioning and isotopic fractionation in the Earth's mantle (Badro, 2014; Lin et al., 2013). Whether bridgmanite undergoes any spin transition under Earth's lower mantle conditions, however, is a question hanging for decades. The Fe^{2+} can only occupy A site in perovskite structure. It was suggested to undergo a high-spin (HS) to low-spin (LS) or HS to intermediate-spin (IS) transition in earlier studies, but recent researches demonstrated that Fe^{2+} shows no spin transition in A site up to at least 120 GPa (reviewed by Badro, 2014). The Fe^{3+} in A site also has no spin transition within the mantle pressure range, but the Fe^{3+} in B site was reported to transform to LS state at 15–50 GPa in multiple studies (Catalli et al., 2010; Fu et al., 2018; Liu et al., 2018; Mao et al., 2015; Okuda et al., 2019). Some studies further argued that HS Fe^{3+} can undergo a cation exchange with Al^{3+} in B site at ~40–80 GPa and high temperature, in which B-site Fe^{3+} will subsequently transform into LS state as discussed above (Catalli et al., 2011; Fujino et al., 2012; Kupenko et al., 2015), but the others did not observe this cation exchange and spin transition (Dubrovinsky et al., 2010; Glazyrin et al., 2014; Potapkin et al., 2013). Theoretical calculations also predicted the Fe-Al cation exchange to be energetically unfavorable due to the large Bader radius of both HS and LS Fe^{3+} (Mohn & Trønnes, 2016). To date, the controversary on the cation exchange-spin transition hypothesis in (Fe, Al)-bearing bridgmanite has not been fully resolved yet.

In this study, we synthesized a new bridgmanite sample with the composition $(Mg_{0.47–0.50}Fe_{0.52})(Al_{0.46–0.47}Si_{0.51–0.55})O_3$, hereafter referred to FA50, and studied its structure, elastic, and electronic properties by X-ray diffraction (XRD), X-ray emission spectroscopy (XES), and synchrotron Mössbauer spectroscopy (SMS) experiments and DFT calculations. With the highest fraction of Fe-Al substitution, we aim to better resolve the potential cation exchange and spin transition under high pressure and high temperature and investigate the influence of Fe-Al incorporation in bridgmanite on the physics and chemistry of the lower mantle.

2. Materials and Methods

2.1. Multianvil Apparatus Synthesis and Characterization

The synthesis was conducted using the 1,000-ton multianvil apparatus (MA) at the University of Michigan. The starting materials were a mixture of MgO, SiO_2, Fe_2O_3, and Al_2O_3 with 2:2:1:1 molar ratio. In the synthesis of ^{57}Fe-enriched sample, half of the Fe_2O_3 was replaced by $^{57}Fe_2O_3$. The mixture was heated at 1,073 K for 8 hr to remove the moisture and structural water before sample loading. The COMPRES 8/3 cell assemblies were used in the synthesis (Leinenweber et al., 2012). The sample was loaded in a platinum capsule and kept at 24 GPa and 1,873 K for 10 hr before quenching to room temperature and then decompressed to 1 bar. The recovered product was examined by JOEL-7800FLV Scanning Electron Microprobe (SEM) and SX-100 Electron Microprobe Analysis (EPMA) at the Electron Microbeam Analysis Laboratory (EMAL) of the University of Michigan. The accelerating voltage and beam current were set at 15 kV and 10 nA. The product consists of mainly $(Mg_{0.5}Fe_{0.5})(Al_{0.5}Si_{0.5})O_3$ (FA50, exact formula $(Mg_{0.50}Fe_{0.52})(Al_{0.47}Si_{0.51})O_3$ and $(Mg_{0.47}Fe_{0.52})(Al_{0.46}Si_{0.55})O_3$ in two independent runs), with minor excess Al_2O_3 and SiO_2, and a coexisting Si-deficient oxide $Mg_{1.47}Fe_{2.46}Al_{1.11}Si_{0.12}O_7$, hereafter referred to MFA (Figure S1 and Table S1 in the supporting information).

2.2. Diamond Anvil Cell Experiments

Diamond anvil cells (DACs) with 150 and 300 μm diameter diamond culets were employed in the synchrotron XRD experiment up to 102 GPa, and XES and SMS experiments up to 80 GPa, respectively. Rhenium gasket was used for the XRD experiment, and beryllium gasket was used for the XES and SMS experiments. XES

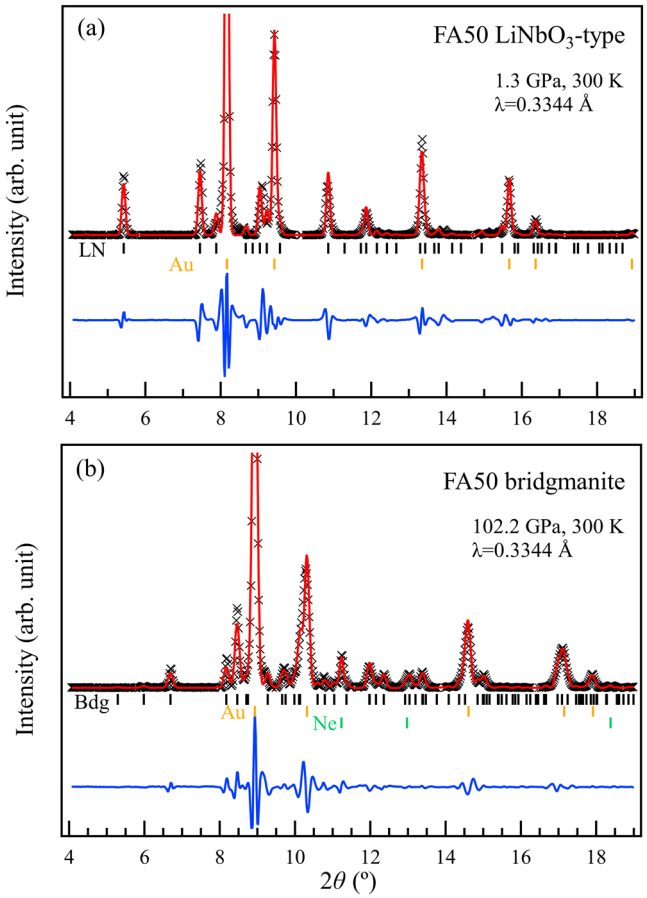

Figure 1. X-ray diffraction patterns of compressed FA50 polymorphs at 300 K. (a) $LiNbO_3$-type (LN) FA50 at 1.3 GPa, 300 K with $a = 4.864(1)$ Å and $c = 12.997(3)$ Å; (b) FA50 bridgmanite (Bdg) at 102.2 GPa, 300 K after laser annealing with $a = 4.385(6)$ Å, $b = 4.690(3)$ Å, and $c = 6.410(13)$ Å. Ticks of gold (Au), neon (Ne), and the residual curve (blue) between experimental data (black cross) and fitted curve (red line) are shown.

and SMS data were collected on the same sample. The gaskets were preindented to ~30 μm thickness. Holes of 90 μm for 150 μm culet and 150 μm for 300 μm culet were drilled by the laser-drilling system at HPCAT of Advanced Photon Source (APS), Argonne National Lab (ANL).

The XRD experiment was conducted at beamline 13-ID-D at APS, ANL. Two sample grains with ~30 μm diameter and ~15 μm thickness were picked from the MA synthesis product and loaded into the sample chamber. Au powder was dispersed into the sample chamber as the pressure calibrant (Fei et al., 2007). Neon gas was loaded as the pressure medium and thermal insulator using the COMPRES/GSECARS gas loading system at APS, ANL. The incident X-ray beam size was ~3 μm in diameter, and the wavelength was 0.3344 Å. A flat-top double-sided laser-heating system, with the beam spot focused to ~30 μm, was used to reach high temperatures (Prakapenka et al., 2008). We scan heated the sample continuously to avoid creating large temperature gradient inside the sample. The two sample grains were first compressed to ~27 GPa and laser annealed at 1,600–1,800 K for 10 min until the XRD showed the sample was fully converted to bridgmanite polycrystalline phase. One sample grain was then further compressed and laser annealed each time after compression to facilitate the potential phase transition and cation exchange. XRD patterns were collected twice before and after laser annealing. The other sample grain was compressed simultaneously without laser annealing for comparison. All XRD patterns used for lattice refinement were collected by applying a ±10° rotation wide scan to improve the number and quality of the peaks. The Au peaks appeared together with the sample peaks in the XRD patterns so the pressure deviation between sample and pressure marker was minimized. Dioptas (Prescher & Prakapenka, 2015), GSAS (Toby, 2001), and PDIndexer (Seto et al., 2010) software were used to integrate and process the XRD data. The lattice parameters were fitted by a Le-Bail method. The sample peaks overlapped with gold or neon peaks were excluded from the fitting.

The XES experiment was conducted at beamline 16-ID-D at APS, ANL. A sample with ~40 μm diameter and ~15 μm thickness was directly loaded into the sample chamber. Silicone oil was used as the pressure medium, and the edge of Raman peak from diamond culet was used for the pressure calibration (Akahama & Kawamura, 2006). The incident X-ray beam size was 5×7 μm^2, and the beam energy is 11.3 keV with a bandwidth of ~1 eV. Fe K_β emission was selected by silicon analyzer and reflected to a silicon detector with an energy step of about 0.3 eV. Each spectrum took ~40 min, and one to three spectra were taken to accumulate at least 30,000 counts at the Fe K_β main peak at each pressure. The sample was laser annealed at 1,300–2,100 K for 15–35 min at 59, 75, and 80 GPa to facilitate the potential phase transition and cation exchange at 13-ID-D, using the same procedure as that in XRD experiments. The time domain SMS measurements were performed on the same sample in XES experiments at beamline 3-ID-B at APS, ANL. The time window of SMS with effective statistics was extended to 250 ns in hybrid mode, providing better constraint on the hyperfine parameter. The incident X-ray beam size was ~20×20 μm^2. Each spectrum was collected for ~12 hr. The CONUSS package was used for the data processing (Sturhahn, 2000).

2.3. Density Functional Theory Calculation

Density functional theory (DFT) calculation was performed using the Vienna ab initio Simulation Package (VASP) in the MedeA software (Kresse & Furthmüller, 1996). Exchange and correlation were treated using PBE-GGA pseudopotential. The energy cutoff was set to 520 eV. The convergence criteria for the self-consistency loop was set to 10^{-5} eV. The k-point grid was set to $6 \times 6 \times 4$ for original bridgmanite lattice and was scaled down by ratio when building the supercells. Spin polarization was included for Fe atom. The

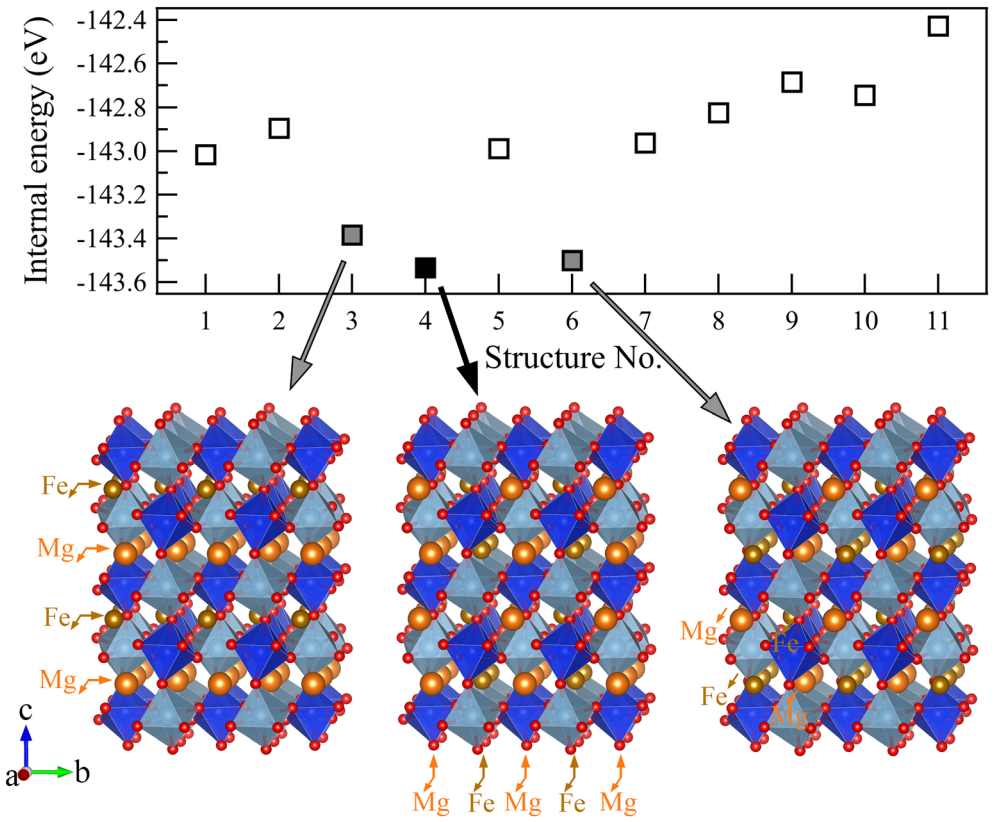

Figure 2. Comparison of internal energy of different cation orderings in FA50 bridgmanite. All structures are calculated at fixed volume of 167.53 Å^3. The most energetically favored structure (4, black filled square) and two close competitors (3 and 6, gray filled squares) share the same type of B-site ordering, in which each Si atom (dark blue spheres and octahedra) is bridged to six Al atoms (light blue spheres and octahedra) by O atoms (red spheres), and vice versa. Structure 4 has an alternating Mg (light brown spheres) and Fe (dark brown spheres) sheet arrangement in *ac* (010) plane along the *b* axis direction. This indicates that the Fe and Al atoms alternate between the closest neighbor sites along the (110) and (1–10) plane normal directions but align separately in column in the (001) plane normal direction.

$MgSiO_3$ bridgmanite structure was used as the prototype, and 11 different types of Fe-Al substitution configurations were selected to search for the most energetically stable structure of $(Mg_{0.5}Fe_{0.5})(Al_{0.5}Si_{0.5})O_3$ bridgmanite.

3. Results and Discussions

3.1. $LiNbO_3$—Bridgmanite Phase Transition

The quenched product FA50 from the MA experiments can be initially indexed as a corundum-type structure at ambient pressure (Figure 1). It transformed into bridgmanite at 18.8 GPa. The bridgmanite phase remained stable from 26.8 to 102.2 GPa after laser-annealing treatment (Figure 1b). The transition to bridgmanite occurred without heating and at ~5 GPa lower than that for pure $MgSiO_3$. Since the sample was synthesized in MA at 24 GPa, which exceeds the transition pressure, the corundum-type phase may have formed retrogressively during decompression. Both the forward and reverse transitions can proceed without heating, implying a low kinetic barrier between the two phases. The low kinetic barrier may be explained by the structures of the perovskite and $LiNbO_3$-type phases, which are related through the rotation of the BX_6 octahedra without breaking B-X bonds (Ross et al., 1989). The *c*/*a* ratio of the quenched sample is 2.67, consistent with the expected value of ~2.63–2.69 for $LiNbO_3$-type ordering (Abrahams & Marsh, 1986; Ko & Prewitt, 1988; Leinenweber et al., 1995) and smaller than those of the corundum prototype at ~2.73 (Blake et al., 1966; Yim & Paff, 1974) or ilmenite-type ordering at ~2.77–2.87 (Horiuchi et al., 1982; Kidoh et al., 1984; Wechsler & Prewitt, 1984). The $LiNbO_3$-type phase is completely ordered between the A and

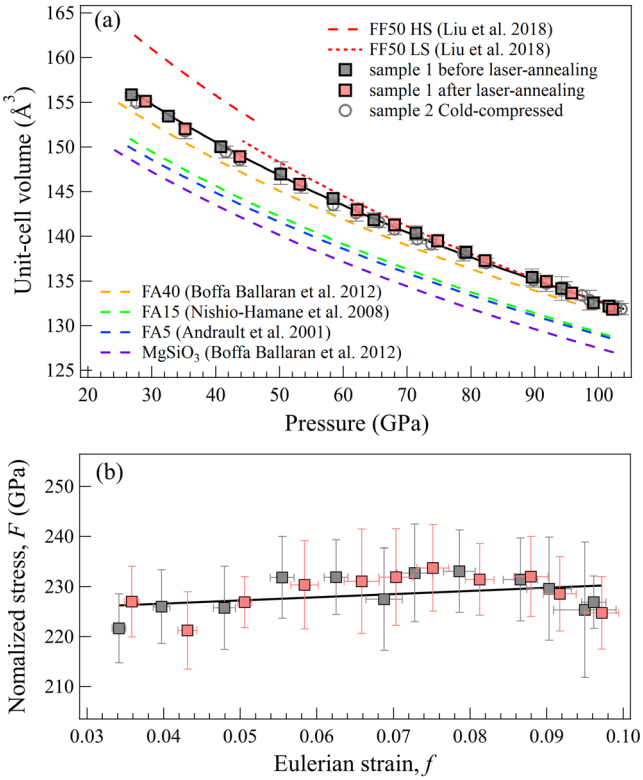

Figure 3. Compression curve of FA50 bridgmanite at 300 K. (a) Unit-cell volume as a function of pressure. Sample 1 (filled squares) was laser annealed after each compression, while Sample 2 (open circles) was cold compressed to the highest pressure. (b) Normalized stress-Eulerian strain (*F-f*) plot. Symbols correspond to those in (a). The data can be fitted linearly with slope close to 0, indicating the validity of using a second-order BM-EoS.

B sites, each consisting of a corner-sharing octahedral framework. One set of corner-sharing framework is fully occupied by Si and Al cations, which rotates to the BX_6 corner-sharing framework of bridgmanite; the other set is occupied by Mg and Fe cations, which displaces to the pseudo-dodecahedral A site in bridgmanite upon compression.

In the FA50 bridgmanite, both A and B sites are occupied by two cations instead of one. To search for the most stable ordering of Mg/Fe in A site and Si/Al in B site, we performed DFT calculations on 11 structures of $(Mg_{0.5}Fe_{0.5})(Al_{0.5}Si_{0.5})O_3$ with different cation arrangements at 0 K. The three energetically favored structures share the same type of Si/Al ordering in B site, in which Si and Al atoms alternate in all axial directions. With this B-site framework, an altered Mg and Si sheet arrangement in *ac* plane along *b* direction is most energetically favorable, while the strip arrangement along *b* direction is the closest competitor with 33 meV higher in internal energy (Figure 2). The $LiNbO_3$-type phase as a retrogressive product should share the same cation framework of bridgmanite. It is worth noting that the complete cation ordering inside A and B sites can be disrupted by the elevated temperature; thus, further experiments are still needed to testify these predicted orderings.

3.2. Equation of State and Spin Transition

The sample grains were heated to 1,600–1,800 K for 10 min at ~27 GPa to release stress and facilitate the formation of bridgmanite from $LiNbO_3$ phase. The two bridgmanite samples were then compressed to ~102 GPa with a 2–7 GPa pressure interval. Previous studies showed that due to kinetic barrier Fe-Al exchange only occurred at high temperature (Catalli et al., 2011; Fujino et al., 2012; Kupenko et al., 2015). Therefore, we laser annealed Sample 1 at 1,600–2,200 K for 10–25 min each time after compression to facilitate cation exchange and phase transition (Figure S2). This sample should always adopt the stable cation ordering at high-pressure and high-temperature conditions at the whole pressure range. Two XRD patterns were collected after each compression, one before and the other after the laser annealing for the laser-annealed sample (gray and red squares in Figure 3). The pressure after laser annealing was higher than that before laser heating, because the pressure was still slowly increasing during heating. We tried to fit the unit-cell volume as a function of pressure by the second-order Birch-Murnaghan equation of state (BM-EoS). Fitting only the data after laser annealing (red squares in Figure 3) yields V_0 = 172.0(7) Å^3, K_0 = 230(6) GPa with K_0' = 4(fixed), while fitting both the data before and after laser annealing (gray and red squares in Figure 3) yields V_0 = 172.1(4) Å^3, K_0 = 229(4) GPa with K_0' = 4(fixed). The two EoSs are almost identical within uncertainty, indicating laser annealing at each pressure points did not introduce visible volume collapse from potential cation exchange and spin transition. Therefore, the second EoS with a denser data coverage and smaller uncertainties was used to represent the EoS for thermodynamically stable structure and ordering of FA50 sample. The slope of normalized stress-Eulerian strain (*F-f*) fitting is almost flat, indicating the validity of fixing K_0' to 4.

Sample 2 was only cold compressed; thus, no cation exchange and spin transition were expected, and it served as a reference for the initial cation ordering. This sample has a similar or slightly lower volume at the whole pressure range with the laser-annealed sample. Its EoS parameters V_0 = 170.7(3) Å^3, K_0 = 240(3) GPa with K_0' = 4(fixed) confirmed this observation. DFT calculations give EoS parameters of V_0 = 176.5(5) A^3, K_0 = 212(12) GPa and K_0' = 3.97(33) from energy-volume fitting, in which the Fe^{3+} is at A site and HS, consistent with the EoS of Sample 2 with a typical overestimation of V_0 and underestimate of K_0. If Sample 1 has a continuous cation exchange and spin transition along with the increased pressure, it should have a lower volume and softened K_0 compared with those of Sample 2. However, the volumes do not show the trend as expectation, suggesting that even if there is any cation exchange and spin transition in Sample 1, it does not introduce visible volume collapse compared with its original state. The bulk modulus of

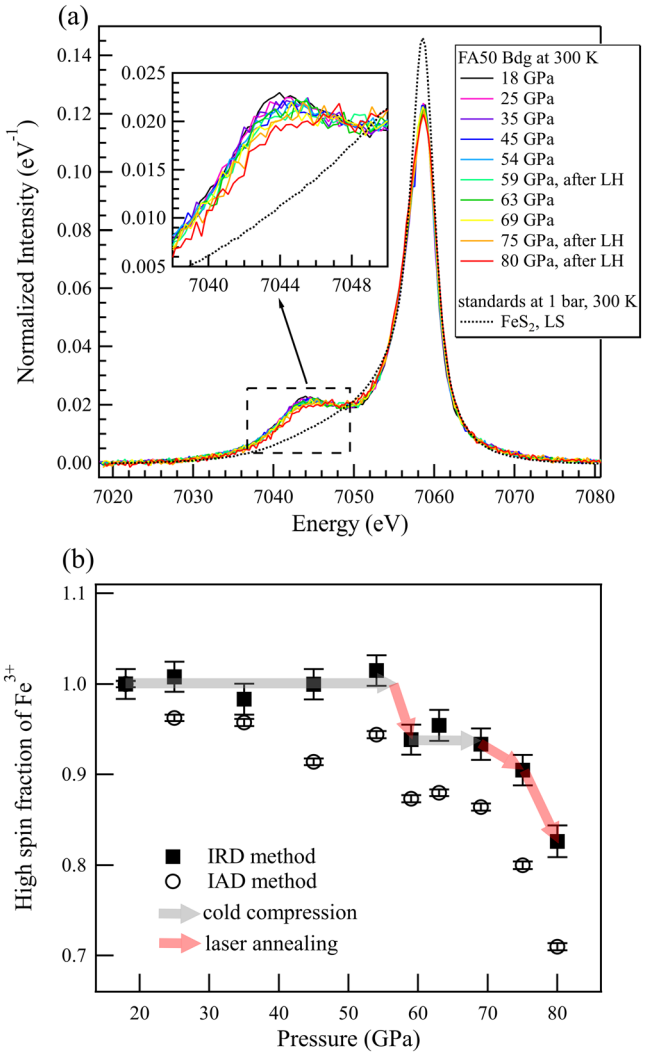

Figure 4. X-ray emission spectroscopy measurements of FA50 bridgmanite at high pressures. (a) XES Fe K_β spectra of FA50 from 18 to 80 GPa, together with the LS (black dotted) reference spectra. The spectra at 18 GPa (black solid) was used as HS reference. All spectra were normalized to unity in integral area and aligned by the position of the K_β main peak. Inset: Fe K_β satellite peak, whose area shrank after laser heating at high pressure, indicating a decrease of HS Fe^{3+} species. (b) The HS fraction of Fe^{3+} calculated by the IAD of the Fe K_β satellite peak (open circles). The IAD method integrates the satellite peak area to the isobestic point around 7,049 eV; for comparison, the IRD method (filled squares) integrates the area at 7,030–7,056 eV, to correct for natural peak broadening at high pressure.

Sample 1 is lower than Sample 2 as expected, but the difference is small and not conclusive enough to determine any transition considering the uncertainty level indicated by the inverse trend in volume. Overall, comparing these two samples could not distinguish any pressure-induced cation exchange and spin transition as suggested in other FA bridgmanite (Catalli et al., 2011; Fujino et al., 2012; Kupenko et al., 2015), indicating either there is no cation exchange or the cation exchange and subsequent spin transition do not introduce resolvable difference by XRD method.

The FA50 bridgmanite has a larger unit-cell volume than $MgSiO_3$ and other Fe,Al-bearing bridgmanite samples with lower Fe-Al contents, due to the large ionic size of Fe^{3+} and Al^{3+} (Andrault et al., 2001; Boffa Ballaran et al., 2012; Nishio-Hamane et al., 2008). Its unit-cell volume is smaller than the $(Mg_{0.46}Fe_{0.53})(Fe_{0.51}Si_{0.49})O_3$ (FF50) bridgmanite (Liu et al., 2018), which indicates Fe^{3+}(HS) > Fe^{3+}(LS) > Al^{3+} in B site. This relation is consistent with the ionic radius at ambient pressure (Shannon, 1976). The gap between FA50 and LS-state FF50 bridgmanite decreases with pressure, indicating Fe^{3+}(LS) is more compressible than Al^{3+} at high pressure. When comparing these Fe-Al substituted bridgmanites at $K_0' = \sim 4$, the unit-cell volumes exhibit a quasi-linear relation with the fraction of Fe-Al substitution (Figure S3). The bulk moduli have a negative correlation to the unit-cell volumes (Table S2) (Andrault et al., 2001; Boffa Ballaran et al., 2012; Liu et al., 2018; Nishio-Hamane et al., 2008) except a small anomaly between $MgSiO_3$ (Boffa Ballaran et al., 2012) and FA5 (Andrault et al., 2001) within uncertainty, consistent with that the larger ion is more compressible.

To further examine spin transition, we performed XES and SMS measurements, which are more sensitive probes for the electronic configuration than XRD, on the FA50 bridgmanite (Figures 4 and 5). The sample was compressed from 18 to 80 GPa and laser heated at three pressures of 59, 75, and 80 GPa. In XES spectra, the area depression of the satellite peak around 7,044 eV was used to quantify the fraction of LS Fe^{3+} in B site. The area difference was calculated by subtracting the spectrum of LS standard from the measured ones, and the spectrum at 18 GPa was set as HS standard. The intensity relative difference (IRD) and intensity absolute difference (IAD) methods were both applied to calculate the area difference (Figure 4b) (Mao et al., 2014). Before laser heating at 18–54 GPa, the areas of the satellite peaks remained similar to HS standard, indicating no spin transition. After the first laser annealing at 59 GPa, the peak area was depressed by ~6%, indicating ~6% Fe^{3+} transformed into LS state (Figure 2b). It also implies the same fraction of Fe^{3+} exchanged into B site. The peak area was further diminished at 75 and 80 GPa where laser-annealing treatment was applied. The good correlation between peak area and laser-annealing treatment indicates that high temperature is necessary to overcome the kinetic barrier during cation-exchange-induced spin transition. The increased fraction of cation exchange with pressure indicates that the transition could happen in a wide pressure range, where the LS-state B-site Fe^{3+} continuously increase with depth (Figure 4b). At 80 GPa after laser annealing, the fraction of LS Fe^{3+} increased to 17–29% from IRD and IAD methods, respectively, implying that the fraction of Fe^{3+} HS-LS transition increases with pressure. The 59 GPa pressure point thus only gave an upper limit of the initiation pressure of the cation exchange and spin transition, while the transition could initiate at lower pressure if been heated. If extrapolated from the pressure-HS fraction of Fe^{3+} at 59, 75, and 80 GPa, the initiation pressure was roughly estimated at ~47 GPa, but the uncertainty is extremely large;

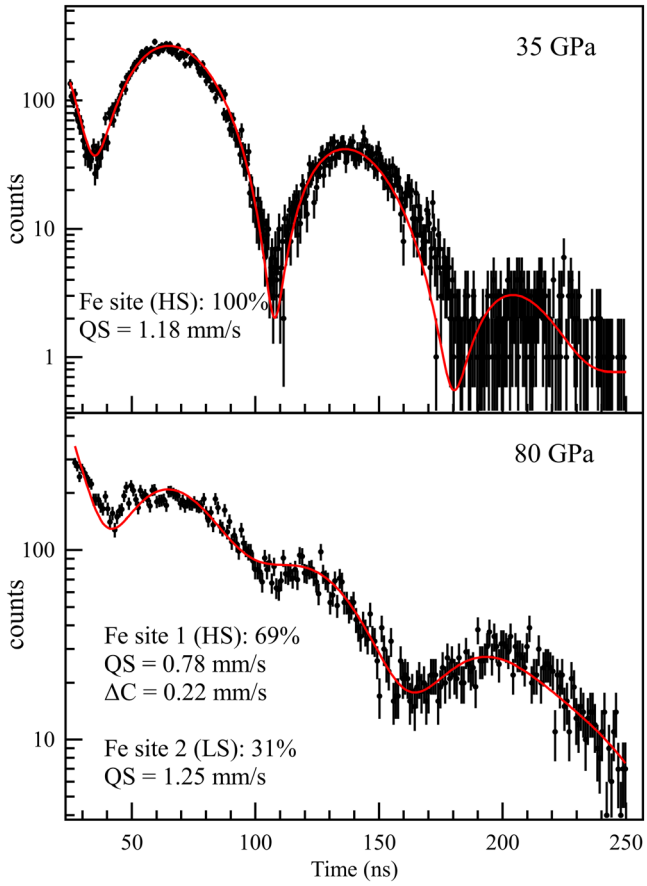

Figure 5. SMS measurements of compressed FA50 bridgmanite after laser heating. At 35 GPa the spectrum can be fitted by one Fe site, which corresponds to the HS Fe^{3+} at the A site. Fitting the spectrum at 80 GPa requires at least two Fe sites: 69% Fe^{3+} with a low quadrupole splitting (QS) was assigned to a HS state, and 31% Fe^{3+} with a high QS was assigned to a LS state (Lin et al., 2012; Liu et al., 2018). The difference in center shift (ΔC) between the two sites is 0.22 mm/s, consistent with the 0.1–0.3 mm/s values for FF50 sample (Liu et al., 2018). The SMS measurements were done on the same sample in XES measurements.

thus, further investigation is needed with denser pressure coverage. In addition, we collected two SMS spectra at 35 and 80 GPa on the same sample before and after laser annealing, which confirmed the magnetic transition (Figure 5). The spectrum at 35 GPa can be well explained by one HS Fe^{3+} site, while the spectrum at 80 GPa needs at least two Fe^{3+} sites for a satisfactory fitting. The fitted Quadrupole Splitting (QS) of Fe^{3+} was consistent with those in previous studies (Lin et al., 2012; Liu et al., 2015). The LS proportion is 31%, consistent with XES measurement within uncertainties. The observed cation-exchange-induced spin transition coincides with several previous studies (Catalli et al., 2011; Fujino et al., 2012; Kupenko et al., 2015) but opposites to the others (Dubrovinsky et al., 2010; Glazyrin et al., 2014; Potapkin et al., 2013). The absence of observation of spin transition in these previous studies may be resulted from the kinetic barrier of cation exchange, or the low signal due to low Fe^{3+} concentration.

The limited fraction of cation exchange and spin transition also explains the absence of volume collapse in XRD results. The volume reduction associated with full transformation of B site Fe^{3+} in $(Mg_{0.5}Fe_{0.5})(Fe_{0.5}Si_{0.5})O_3$ into the LS state is estimated at ~0.5% (Liu et al., 2018). In our sample, if 20% of the Fe^{3+} enters the B site after laser annealing, the transformation of $(Mg_{0.5}Fe_{0.4}Al_{0.1})(Fe_{0.1}Al_{0.4}Si_{0.5})O_3$ to the LS state at ~80 GPa would produce ~0.1% volume reduction (~0.14 $Å^3$), well below the uncertainty level of volume refinement. The volume reduction would be even smaller in the Earth's mantle, which typically has much lower Fe-Al contents (Boffa Ballaran et al., 2012; Glazyrin et al., 2014).

3.3. Bulk Sound Velocity

Although the spin transition in Fe-Al bridgmanite is likely seismically invisible, the compositional difference between Fe-Al bridgmanite and $MgSiO_3$ bridgmanite results in significant contrast in their density and compressibility, which leads to the difference in bulk sound velocity:

$$v_\Phi = \sqrt{K/\rho} = \sqrt{KV/M}, \quad (1)$$

where ρ is density and M and V are the unit-cell mass and volume, respectively. Figure 6 plotted v_Φ of different bridgmanites as a function of pressure. The v_Φ can also be calculated from the direct sound velocity measurement by

$$v_\Phi = \sqrt{v_p{}^2 - \frac{4}{3}v_s{}^2}, \quad (2)$$

where v_p is the compressional wave velocity and v_s is the shear wave velocity.

The v_Φ decreases systematically with increased Fe-Al content in these bridgmanites, because the differences of v_Φ mainly come from the unit-cell mass difference introduced by Fe substitution. The K and V of these bridgmanites are anticorrelated with each other as discussed above, making the KV term close in value for different bridgmanite and the M the dominant factor for the difference in v_Φ. For example, at 130 GPa, $MgSiO_3$ and FA50 have only −1.6% difference in KV, but a constant 15.5% difference in M; the v_Φ of FA50 is about 7.7% smaller than that of $MgSiO_3$ bridgmanite, and this difference is dominated by the difference in M (Figure 6). Thus, from the mass difference, FA50 might represent the highest sound velocity variation introduced by the coupled Fe-Al substitution. v_Φ of FF50 is ~16.4% smaller than that of $MgSiO_3$ bridgmanite at 130 GPa (Liu et al., 2018), which means substituting 50% Fe in B site further reduce bulk sound velocity by

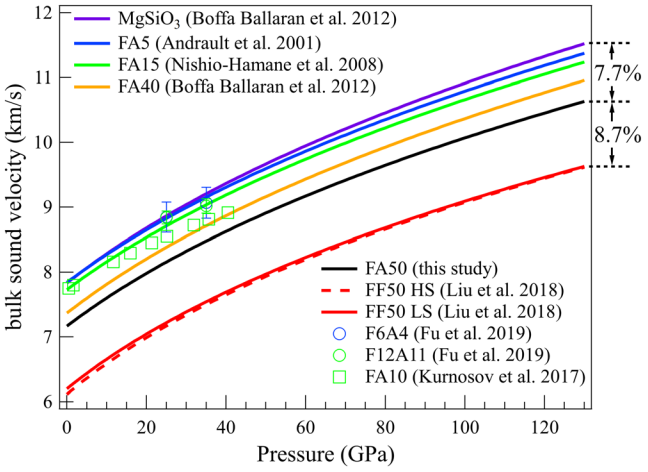

Figure 6. Calculated bulk sound velocity of FA50 bridgmanite. The bulk sound velocity shows a negative correlation with its Fe^{3+}content, mainly because the atomic mass of Fe is about twice as heavy as that of Mg, Al, or Si. At 130 GPa and 300 K, the bulk sound velocity of $MgSiO_3$ is 7.7% higher than that of FA50 bridgmanite (50% Fe^{3+} in A site), which in turn is 8.7% higher than that of FF50 bridgmanite (additional 50% Fe^{3+} in B site).

~8.7%, quite similar to substituting 50% Fe in A site. Therefore, the incorporation of Fe^{3+} into either/both sites decreases v_Φ equally by ~8.2% for each 0.25 $Fe^{3+}/(Fe^{3+}+Mg+Si+Al)$, at core-mantle boundary pressure, which can serve as a criterion on detecting Fe-enriched region in lower mantle. The similar volume deduction for A and B sites also implies that a significant sound velocity discontinuity is not expected during cation exchange.

When comparing the v_Φ derived from sound velocity measurement with the v_Φ calculated from EoS parameters of similar compositions, the F6A4 and F12A11 composition matches well with the range defined by FA5 and FA15 (Fu et al., 2019), but the FA10 showed a different slope with increased pressure, mainly because the K' is 3.44(3), lower than those in other studies (Kurnosov et al., 2017). It is still acceptable difference concerning the uncertainty range in sound velocity measurements. Previous study also suggested that Fe^{3+}, if originally HS at B site, can induce sound velocity discontinuity during spin transition due to the softening of bulk modulus K (Fu et al., 2018). It is a different scenario for Fe-Al substituted bridgmanite where Fe^{3+} is located at A site originally and the spin transition requires cation exchange. Although the Fe^{3+} turns to LS state immediately after entering B site at >15–50 GPa (Catalli et al., 2010; Fu et al., 2018; Liu et al., 2018; Mao et al., 2015; Okuda et al., 2019), the cation exchange itself is a gradual process with increased pressure throughout the whole lower mantle, which controls the fraction of LS Fe^{3+}. Therefore, the changes resulted from the cation exchange and spin transition are distributed into the whole lower mantle pressure, and a volume collapse or a bulk modulus softening is not expected to occur within a narrow pressure range. We thus posit that the spin transition in Fe-Al coupled bridgmanite does not cause a resolvable seismic discontinuity in Earth's mantle.

4. Implications and Conclusions

The prediction of Fe^{2+} disproportionation in bridgmanite (Frost et al., 2004) and the positive correlation between Fe^{3+} and Al content in bridgmanite composition silicates from diamond inclusions (McCammon et al., 1997) imply that Fe-Al coupled substitution may be a major mechanism to accommodate Fe and Al in lower mantle. The solubility of Fe-Al in $MgSiO_3$ bridgmanite was suggested to have an upper limit since $FeAlO_3$ stabilizes as Rh_2O_3(II) instead of the perovskite structure (Nagai et al., 2005; Nishio-Hamane et al., 2005). Previous studies reported the synthesis of a series of bridgmanites ranging from FA5 to FA40 (Andrault et al., 2001; Boffa Ballaran et al., 2012; Nishio-Hamane et al., 2008). Here the synthesis of FA50 further elevates this upper limit of solubility to 50%, which may be an end member of this bridgmanite series. More interestingly, FA50 may have different cation ordering from FA5-40 because FA50 can transform into a $LiNbO_3$-type phase reversibly, while FA5-FA40 did not have similar transition and therefore always quenched as metastable bridgmanite. The difference may be explained by the cation arrangement is more ordered in FA50, possibly due to the nearly 1:1 stoichiometric ratio of $MgSiO_3$ and $FeAlO_3$. Although complete ordering inside A and B sites is unlikely at mantle temperatures, a more ordered cation arrangement may have lower entropy and would be energetically favored under lower temperatures. Considering that both FA50 and $MgSiO_3$ bridgmanite have lower entropy than the bridgmanites with intermediate composition, the FA5-FA40 may decompose into FA50 and $MgSiO_3$ end members in order to minimize the total free energy in low-temperature environments such as cold subducted slabs, which is also an environment enriched with Fe^{3+}.

With the extreme iron enrichment in FA50 sample, we observed a gradual increase of the fraction of B site LS Fe^{3+} in Fe-Al coupled substitution bridgmanite due to Fe-Al cation exchange. The spin transition, however, does not induce a sharp unit-cell volume reduction or bulk modulus softening, thus may not be able to introduce detectable seismic anomaly at specific pressure. It has also been suggested that Fe-Al coupled incorporation has very limited influence on its electrical conductivity because it does not introduce site vacancy in bridgmanite that enhances the conductivity (Potapkin et al., 2013; Sinmyo et al., 2014). The HS-LS transition in FF50 only lowers the electrical conductivity by <0.3 log unit (Liu et al., 2018). Since

the Fe-Al site exchange in FA50 does not introduce additional defects from charge balance and the amount of Fe^{3+} in B-site is less than FF50, the spin transition may also be difficult to be detected by electromagnetic probes.

Isotopic fractionation of Fe in the lower mantle may be affected by the spin transition of Fe^{3+}- and Al^{3+}-bearing bridgmanite. When Fe^{3+} exchanges with Al^{3+} to enter the B site and undergoes spin transition, the Fe-O bond shortens, and the coordination number decreases from 8 to 6. As the Fe-O bond in bridgmanite becomes stiffer with increasing depth, heavier Fe isotopes may be favored in bridgmanite, as suggested by previous studies of isotopic fractionation associated with spin transition in ferropericlase, Fe^{2+}-bearing bridgmanite, and phase transition in metallic iron alloys (Lai et al., 2017; Rustad & Yin, 2009). The increased fraction of B-site Fe^{3+} with pressure may result in a chemical heterogeneity with depth. Further investigations are needed from high-pressure experiments to test if the isotopic fractionation fits this prediction and makes it a potential depth indicator for volcanic products and deep mantle diamond inclusions.

The B-site Fe^{3+} spin transition may also affect the iron partitioning between bridgmanite and ferropericlase (Lin et al., 2013). However, the Fe in ferropericlase is dominantly Fe^{2+}, and therefore, Fe-Mg repartitioning between ferropericlase and Fe^{3+}-bearing bridgmanite would require oxidizing or reducing source. In Earth's mantle, the metallic Fe^{0} produced from Fe^{2+} disproportionation (Frost et al., 2004) can be a reducing source to partition more Fe into ferropericlase during spin transition; conversely, the disproportionation reaction may produce additional Fe^{3+} to enter bridgmanite, which serves as an additional oxidizing source. Therefore, the cation exchange and spin transition can influence the Fe partitioning between Fe-Al bridgmanite and ferropericlase in the Earth's mantle; meanwhile, this process may also slightly change the redox state of lower mantle.

Data Availability Statement

All the data to produce the results are available on Zenodo (http://doi.org/10.5281/zenodo.3747000).

Acknowledgments

J. L. acknowledges support from NSF EAR-1763189 and NASA NNX15AG54G. B. C. acknowledges support from NSF EAR-1555388, EAR-1565708, and EAR-1829273. We thank Dr. Li Zhang for discussions and two anonymous reviewers for comments. XRD, XES, and SMS experiments used resources of the Advanced Photon Source, a U.S. Department of Energy (DOE) Office of Science User Facility operated for the DOE Office of Science by Argonne National Laboratory under Contract DE-AC02-06CH11357. The XRD experiments were performed at GeoSoilEnviroCARS (The University of Chicago, Sector 13), Advanced Photon Source (APS), Argonne National Laboratory. GeoSoilEnviroCARS is supported by the National Science Foundation-Earth Sciences (EAR-1634415) and Department of Energy-GeoSciences (DE-FG02-94ER14466). Use of the COMPRES-GSECARS gas loading system was supported by COMPRES under NSF Cooperative Agreement EAR-1606856 and by GSECARS through NSF Grant EAR-1634415 and DOE Grant DE-FG02-94ER14466. XES experiments were performed at HPCAT (Sector 16), Advanced Photon Source (APS), Argonne National Laboratory. HPCAT operations are supported by DOE-NNSA's Office of Experimental Sciences.

References

Abrahams, S., & Marsh, P. (1986). Defect structure dependence on composition in lithium niobate. *Acta Crystallographica Section B: Structural Science*, *42*(1), 61–68. https://doi.org/10.1107/S0108768186098567

Akahama, Y., & Kawamura, H. (2006). Pressure calibration of diamond anvil Raman gauge to 310 GPa. *Journal of Applied Physics*, *100*(4). https://doi.org/10.1063/1.2335683

Andrault, D., Bolfan-Casanova, N., & Guignot, N. (2001). Equation of state of lower mantle (Al,Fe)-$MgSiO_3$ perovskite. *Earth and Planetary Science Letters*, *193*(3–4), 501–508. https://doi.org/10.1016/S0012-821X(01)00506-4

Badro, J. (2014). Spin transitions in mantle minerals. *Annual Review of Earth and Planetary Sciences*, *42*(1), 231–248. https://doi.org/10.1146/annurev-earth-042711-105304

Blake, R., Hessevick, R., Zoltai, T., & Finger, L. W. (1966). Refinement of the hematite structure. *American Mineralogist: Journal of Earth and Planetary Materials*, *51*(1–2), 123–129.

Boffa Ballaran, T., Kurnosov, A., Glazyrin, K., Frost, D. J., Merlini, M., Hanfland, M., & Caracas, R. (2012). Effect of chemistry on the compressibility of silicate perovskite in the lower mantle. *Earth and Planetary Science Letters*, *333*, 181–190. https://doi.org/10.1016/j.epsl.2012.03.029

Catalli, K., Shim, S.-H., Dera, P., Prakapenka, V. B., Zhao, J., Sturhahn, W., et al. (2011). Effects of the Fe^{3+} spin transition on the properties of aluminous perovskite—New insights for lower-mantle seismic heterogeneities. *Earth and Planetary Science Letters*, *310*(3–4), 293–302. https://doi.org/10.1016/j.epsl.2011.08.018

Catalli, K., Shim, S.-H., Prakapenka, V. B., Zhao, J., Sturhahn, W., Chow, P., et al. (2010). Spin state of ferric iron in $MgSiO_3$ perovskite and its effect on elastic properties. *Earth and Planetary Science Letters*, *289*(1–2), 68–75. https://doi.org/10.1016/j.epsl.2009.10.029

Dubrovinsky, L., Boffa-Ballaran, T., Glazyrin, K., Kurnosov, A., Frost, D., Merlini, M., et al. (2010). Single-crystal X-ray diffraction at megabar pressures and temperatures of thousands of degrees. *High Pressure Research*, *30*(4), 620–633. https://doi.org/10.1080/08957959.2010.534092

Fei, Y., Ricolleau, A., Frank, M., Mibe, K., Shen, G., & Prakapenka, V. (2007). Toward an internally consistent pressure scale. *Proceedings of the National Academy of Sciences*, *104*(22), 9182–9186. https://doi.org/10.1073/pnas.0609013104

Frost, D. J., Liebske, C., Langenhorst, F., McCammon, C. A., Trønnes, R. G., & Rubie, D. C. (2004). Experimental evidence for the existence of iron-rich metal in the Earth's lower mantle. *Nature*, *428*(6981), 409–412. https://doi.org/10.1038/nature02413

Fu, S., Yang, J., Tsujino, N., Okuchi, T., Purevjav, N., & Lin, J.-F. (2019). Single-crystal elasticity of (Al, Fe)-bearing bridgmanite and seismic shear wave radial anisotropy at the topmost lower mantle. *Earth and Planetary Science Letters*, *518*, 116–126. https://doi.org/10.1016/j.epsl.2019.04.023

Fu, S., Yang, J., Zhang, Y., Okuchi, T., McCammon, C., Kim, H. I., et al. (2018). Abnormal elasticity of Fe-bearing bridgmanite in the Earth's lower mantle. *Geophysical Research Letters*, *45*, 4725–4732. https://doi.org/10.1029/2018GL077764

Fujino, K., Nishio-Hamane, D., Seto, Y., Sata, N., Nagai, T., Shinmei, T., et al. (2012). Spin transition of ferric iron in Al-bearing Mg-perovskite up to 200GPa and its implication for the lower mantle. *Earth and Planetary Science Letters*, *317*, 407–412. https://doi.org/10.1016/j.epsl.2011.12.006

Glazyrin, K., Ballaran, T. B., Frost, D., McCammon, C., Kantor, A., Merlini, M., et al. (2014). Magnesium silicate perovskite and effect of iron oxidation state on its bulk sound velocity at the conditions of the lower mantle. *Earth and Planetary Science Letters*, *393*, 182–186. https://doi.org/10.1016/j.epsl.2014.01.056

Horiuchi, H., Hirano, M., Ito, E., & Matsui, Y. (1982). $MgSiO_3$ (ilmenite-type): Single crystal X-ray diffraction study. *American Mineralogist*, *67*(7–8), 788–793.

Kidoh, K., Tanaka, K., Marumo, F., & Takei, H. (1984). Electron density distribution in ilmenite-type crystals. II. Manganese (II) titanium (IV) trioxide. *Acta Crystallographica Section B: Structural Science*, *40*(4), 329–332. https://doi.org/10.1107/S0108768184002238

Ko, J., & Prewitt, C. T. (1988). High-pressure phase transition in $MnTiO_3$ from the ilmenite to the $LiNbO_3$ structure. *Physics and Chemistry of Minerals*, *15*(4), 355–362. https://doi.org/10.1007/BF00311040

Kresse, G., & Furthmüller, J. (1996). Software VASP, Vienna (1999). *Physical Review B*, *54*(11), 169.

Kupenko, I., McCammon, C., Sinmyo, R., Cerantola, V., Potapkin, V., Chumakov, A., et al. (2015). Oxidation state of the lower mantle: In situ observations of the iron electronic configuration in bridgmanite at extreme conditions. *Earth and Planetary Science Letters*, *423*, 78–86. https://doi.org/10.1016/j.epsl.2015.04.027

Kurnosov, A., Marquardt, H., Frost, D., Ballaran, T. B., & Ziberna, L. (2017). Evidence for a Fe^{3+}-rich pyrolitic lower mantle from (Al, Fe)-bearing bridgmanite elasticity data. *Nature*, *543*(7646), 543–546. https://doi.org/10.1038/nature21390

Lai, X., Chen, B., Wang, J., Kono, Y., & Zhu, F. (2017). Polyamorphic transformations in Fe-Ni-C liquids: Implications for chemical evolution of terrestrial planets. *Journal of Geophysical Research: Solid Earth*, *122*, 9745–9754. https://doi.org/10.1002/2017JB014835

Leinenweber, K., Linton, J., Navrotsky, A., Fei, Y., & Parise, J. (1995). High-pressure perovskites on the join $CaTiO_3$-$FeTiO_3$. *Physics and Chemistry of Minerals*, *22*(4), 251–258. https://doi.org/10.1007/bf00202258

Leinenweber, K. D., Tyburczy, J. A., Sharp, T. G., Soignard, E., Diedrich, T., Petuskey, W. B., et al. (2012). Cell assemblies for reproducible multi-anvil experiments (the COMPRES assemblies). *American Mineralogist*, *97*(2–3), 353–368. https://doi.org/10.2138/am.2012.3844

Lin, J.-F., Alp, E. E., Mao, Z., Inoue, T., McCammon, C., Xiao, Y., et al. (2012). Electronic spin states of ferric and ferrous iron in the lower-mantle silicate perovskite. *American Mineralogist*, *97*(4), 592–597. https://doi.org/10.2138/am.2012.4000

Lin, J.-F., Speziale, S., Mao, Z., & Marquardt, H. (2013). Effects of the electronic spin transitions of iron in lower mantle minerals: Implications for deep mantle geophysics and geochemistry. *Reviews of Geophysics*, *51*, 244–275. https://doi.org/10.1002/rog.20010

Liu, J., Dorfman, S. M., Zhu, F., Li, J., Wang, Y., Zhang, D., et al. (2018). Valence and spin states of iron are invisible in Earth's lower mantle. *Nature Communications*, *9*(1), 1284. https://doi.org/10.1038/s41467-018-03671-5

Liu, J., Mysen, B., Fei, Y., & Li, J. (2015). Recoil-free fractions of iron in aluminous bridgmanite from temperature-dependent Mössbauer spectra. *American Mineralogist*, *100*(8–9), 1978–1984. https://doi.org/10.2138/am-2015-5245

Mao, Z., Lin, J.-F., Yang, J., Inoue, T., & Prakapenka, V. B. (2015). Effects of the Fe^{3+} spin transition on the equation of state of bridgmanite. *Geophysical Research Letters*, *42*, 4335–4342. https://doi.org/10.1002/2015GL064400

Mao, Z., Lin, J.-F., Yang, J., Wu, J., Watson, H. C., Xiao, Y., et al. (2014). Spin and valence states of iron in Al-bearing silicate glass at high pressures studied by synchrotron Mössbauer and X-ray emission spectroscopy. *American Mineralogist*, *99*(2–3), 415–423. https://doi.org/10.2138/am.2014.4490

McCammon, C., Hutchison, M., & Harris, J. (1997). Ferric iron content of mineral inclusions in diamonds from Sao Luiz: A view into the lower mantle. *Science*, *278*(5337), 434–436. https://doi.org/10.1126/science.278.5337.434

Mohn, C. E., & Trønnes, R. G. (2016). Iron spin state and site distribution in FeAlO3-bearing bridgmanite. *Earth and Planetary Science Letters*, *440*, 178–186. https://doi.org/10.1016/j.epsl.2016.02.010

Nagai, T., Hamane, D., Devi, P. S., Miyajima, N., Yagi, T., Yamanaka, T., & Fujino, K. (2005). A new polymorph of $FeAlO_3$ at high pressure. *The Journal of Physical Chemistry B*, *109*(39), 18226–18229. https://doi.org/10.1021/jp054409s

Nishio-Hamane, D., Nagai, T., Fujino, K., Seto, Y., & Takafuji, N. (2005). Fe^{3+} and Al solubilities in $MgSiO_3$ perovskite: Implication of the Fe^{3+} AlO_3 substitution in $MgSiO_3$ perovskite at the lower mantle condition. *Geophysical Research Letters*, *32*, L16306. https://doi.org/10.1029/2005GL023529

Nishio-Hamane, D., Seto, Y., Fujino, K., & Nagai, T. (2008). Effect of $FeAlO_3$ incorporation into $MgSiO_3$ on the bulk modulus of perovskite. *Physics of the Earth and Planetary Interiors*, *166*(3–4), 219–225. https://doi.org/10.1016/j.pepi.2008.01.002

Okuda, Y., Ohta, K., Sinmyo, R., Hirose, K., Yagi, T., & Ohishi, Y. (2019). Effect of spin transition of iron on the thermal conductivity of (Fe, Al)-bearing bridgmanite. *Earth and Planetary Science Letters*, *520*, 188–198. https://doi.org/10.1016/j.epsl.2019.05.042

Potapkin, V., McCammon, C., Glazyrin, K., Kantor, A., Kupenko, I., Prescher, C., et al. (2013). Effect of iron oxidation state on the electrical conductivity of the Earth's lower mantle. *Nature Communications*, *4*(1), 1427. https://doi.org/10.1038/ncomms2436

Prakapenka, V., Kubo, A., Kuznetsov, A., Laskin, A., Shkurikhin, O., Dera, P., et al. (2008). Advanced flat top laser heating system for high pressure research at GSECARS: Application to the melting behavior of germanium. *High Pressure Research*, *28*(3), 225–235. https://doi.org/10.1080/08957950802050718

Prescher, C., & Prakapenka, V. B. (2015). DIOPTAS: A program for reduction of two-dimensional X-ray diffraction data and data exploration. *High Pressure Research*, *35*(3), 223–230. https://doi.org/10.1080/08957959.2015.1059835

Ross, N. L., Ko, J., & Prewitt, C. T. (1989). A new phase transition in $MnTiO_3$: $LiNbO_3$-perovskite structure. *Physics and Chemistry of Minerals*, *16*(7), 621–629. https://doi.org/10.1007/bf00223309

Rustad, J. R., & Yin, Q.-Z. (2009). Iron isotope fractionation in the Earth's lower mantle. *Nature Geoscience*, *2*(7), 514–518. https://doi.org/10.1038/ngeo546

Seto, Y., Nishio-Hamane, D., Nagai, T., & Sata, N. (2010). Development of a software suite on X-ray diffraction experiments. *Review of High Pressure Science and Technology*, *20*(3), 269–276. https://doi.org/10.4131/jshpreview.20.269

Shannon, R. D. (1976). Revised effective ionic radii and systematic studies of interatomic distances in halides and chalcogenides. *Acta Crystallographica, Section A: Crystal Physics, Diffraction, Theoretical and General Crystallography*, *32*(5), 751–767. https://doi.org/10.1107/S0567739476001551

Sinmyo, R., Pesce, G., Greenberg, E., McCammon, C., & Dubrovinsky, L. (2014). Lower mantle electrical conductivity based on measurements of Al,Fe-bearing perovskite under lower mantle conditions. *Earth and Planetary Science Letters*, *393*, 165–172. https://doi.org/10.1016/j.epsl.2014.02.049

Sturhahn, W. (2000). CONUSS and PHOENIX: Evaluation of nuclear resonant scattering data. *Hyperfine Interactions*, *125*(1/4), 149–172. https://doi.org/10.1023/A:1012681503686

Toby, B. H. (2001). EXPGUI, a graphical user interface for GSAS. *Journal of Applied Crystallography*, *34*(2), 210–213. https://doi.org/10.1107/S0021889801002242

Tschauner, O., Ma, C., Beckett, J. R., Prescher, C., Prakapenka, V. B., & Rossman, G. R. (2014). Discovery of bridgmanite, the most abundant mineral in Earth, in a shocked meteorite. *Science*, *346*(6213), 1100–1102. https://doi.org/10.1126/science.1259369

Wang, X., Tsuchiya, T., & Hase, A. (2015). Computational support for a pyrolitic lower mantle containing ferric iron. *Nature Geoscience*, *8*(7), 556–559. https://doi.org/10.1038/ngeo2458

Wechsler, B. A., & Prewitt, C. T. (1984). Crystal structure of ilmenite ($FeTiO_3$) at high temperature and at high pressure. *American Mineralogist*, *69*(1–2), 176–185.

Yim, W., & Paff, R. (1974). Thermal expansion of AlN, sapphire, and silicon. *Journal of Applied Physics*, *45*(3), 1456–1457. https://doi.org/10.1063/1.1663432